Journal of Advanced Ceramics
2021, **10**(6): 1243–1255
https://doi.org/10.1007/s40145-021-0499-5

ISSN 2226-4108
CN 10-1154/TQ

Research Article

Enhanced giant dielectric properties and improved nonlinear electrical response in acceptor–donor (Al^{3+}, Ta^{5+})-substituted $CaCu_3Ti_4O_{12}$ ceramics

Jakkree BOONLAKHORN[a], Narong CHANLEK[b], Jedsada MANYAM[c], Pornjuk SREPUSHARAWOOT[a,d], Sriprajak KRONGSUK[a,d], Prasit THONGBAI[a,d,*]

[a]*Giant Dielectric and Computational Design Research Group (GD–CDR), Department of Physics, Faculty of Science, Khon Kaen University, Khon Kaen 40002, Thailand*
[b]*Synchrotron Light Research Institute (Public Organization), 111 University Avenue, Muang District, Nakhon Ratchasima 30000, Thailand*
[c]*National Nanotechnology Center (NANOTEC), National Science and Technology Development Agency (NSTDA), Pathum Thani 12120, Thailand*
[d]*Institute of Nanomaterials Research and Innovation for Energy (IN-RIE), NANOTEC-KKU RNN on Nanomaterials Research and Innovation for Energy, Khon Kaen University, Khon Kaen 40002, Thailand*

Received: February 27, 2021; Revised: April 20, 2021; Accepted: May 9, 2021

Abstract: The giant dielectric behavior of $CaCu_3Ti_4O_{12}$ (CCTO) has been widely investigated owing to its potential applications in electronics; however, the loss tangent ($\tan\delta$) of this material is too large for many applications. A partial substitution of CCTO ceramics with either Al^{3+} or Ta^{5+} ions generally results in poorer nonlinear properties and an associated increase in $\tan\delta$ (to ~0.29–1.15). However, first-principles calculations showed that self-charge compensation occurs between these two dopant ions when co-doped into Ti^{4+} sites, which can improve the electrical properties of the grain boundary (GB). Surprisingly, in this study, a greatly enhanced breakdown electric field (~200–6588 V/cm) and nonlinear coefficient (~4.8–15.2) with a significantly reduced $\tan\delta$ (~0.010–0.036) were obtained by simultaneous partial substitution of CCTO with acceptor–donor (Al^{3+}, Ta^{5+}) dopants to produce (Al^{3+}, Ta^{5+})–CCTO ceramics. The reduced $\tan\delta$ and improved nonlinear properties were attributed to the synergistic effects of the co-dopants in the doped CCTO structure. The significant reduction in the mean grain size of the (Al^{3+}, Ta^{5+})–CCTO ceramics compared to pure CCTO was mainly because of the Ta^{5+} ions. Accordingly, the increased GB density due to the reduced grain size and the larger Schottky barrier height (Φ_b) at the GBs of the co-doped CCTO ceramics were the main reasons for the greatly increased GB resistance, improved nonlinear properties, and reduced $\tan\delta$ values compared to pure and single-doped CCTO. In addition, high dielectric constant values ($\varepsilon' \approx (0.52–2.7) \times 10^4$) were obtained. A fine-grained microstructure with highly insulating GBs was obtained by Ta^{5+} doping, while co-doping with Ta^{5+} and Al^{3+} resulted in a high Φ_b. The obtained results are expected to provide useful guidelines for developing new giant dielectric ceramics with excellent dielectric properties.

Keywords: $CaCu_3Ti_4O_{12}$ (CCTO); impedance spectroscopy; nonlinear electrical properties; dielectric constant; loss tangent; first-principles calculations

* Corresponding author.
E-mail: pthongbai@kku.ac.th

1 Introduction

The giant dielectric properties (GDPs) of dielectric materials with a high dielectric constant (ε') have been extensively studied for use in electronics applications, such as capacitive devices used in high-energy storage devices [1–13]. Most recently, giant dielectric materials have been proposed as potential epsilon-negative or mu-negative materials [14–16]. High ε' values of ~10^3–10^5 in the low-frequency range without detectable phase transitions have been reported for a wide range of functional electroceramics, such as doped TiO_2 [4,17], doped SnO_2 [18], doped NiO [19], $CaCu_3Ti_4O_{12}$ (CCTO) and its related structures [3,5,20–23], and $La_{2-x}Sr_xNiO_4$ [24]. These ceramic oxides can be used in electronic devices, such as capacitors, sensors, and varistors. However, these materials still have several serious limitations that restrict their use in electronic devices. The most critical challenge is the high loss tangent ($\tan\delta$) of these materials [4,5,18,20,21]. Furthermore, for use in capacitor applications, a low frequency- and temperature-dependence of ε' (at 1 kHz) is important [4,5].

In addition to potential applications, the primary mechanisms of the GDPs have been widely investigated. The surface/internal barrier layer capacitor (SBLC/IBLC) model [18,20,25], polaron-hopping model [24], electron pinned defect dipole (EPPD) model [4], and non-ohmic sample–electrode contact model [26] have been used to describe the contributions to the GDPs in simple and complex oxides. However, the origin of the GDPs of these dielectric oxides is still unclear and is a current research focus.

In recent years, the dielectric properties of a range of ceramic materials have been improved by substituting pairs of metal ions into their crystalline structures [1,4,5,17,18,27]. Newly discovered A^{3+} (Al^{3+}, In^{3+}, Ga^{3+}) and B^{5+} (Nb^{5+}, Ta^{5+}) acceptor–donor co-doped rutile TiO_2 and SnO_2 ceramics were reported to show GDPs with very low $\tan\delta$ [4,17,18,28]. Hu *et al.* [4] reported the GDPs of (In^{3+}, Nb^{5+}) co-doped rutile TiO_2 ceramics with a very large ε' of ~6×10^4 and very low $\tan\delta$ of ~0.02 at ~25 ℃ room temperature (RT). The EPPD model was used to describe the origin of the greatly enhanced dielectric properties of (In^{3+}, Nb^{5+}) co-doped rutile TiO_2 ceramics [4]. The GDPs of rutile SnO_2 can also be improved by donor–acceptor substitution into the cation sites. Large ε' values of ~10^3 and very low $\tan\delta$ of ~0.03 at RT and low frequency were measured in (Al^{3+}, Nb^{5+}) co-doped rutile SnO_2 ceramics, and the IBLC model was used to describe the primary origin of the GDPs in co-doped SnO_2 ceramics [18]. However, to obtain the GDPs with large ε' and low $\tan\delta$ values in SnO_2- and TiO_2-based ceramics, the materials required sintering at high temperature (1300–1500 ℃) [4,18,28].

This study aimed to apply the co-doped A^{3+} and B^{5+} acceptor–donor concept to produce CCTO at a lower processing temperature than used in previous studies. The acceptor–donor dopants were introduced into the CCTO ceramics via a solid-state reaction (SSR) method and sintering at 1090 ℃. The GDPs of the CCTO ceramics were evaluated, including the nonlinear current density as a function of the electric field (*J*–*E* properties). We hypothesize that these dopants will decrease the $\tan\delta$ of the CCTO by enhancing the electrical properties of the grain boundary (GB). Accordingly, the nonlinear electrical properties will also be improved, while the lower sintering temperature will reduce the energy consumption and cost of processing.

2 Experimental

The SSR method was used to prepare ceramic powders of pure CCTO and doped CCTO that was partially substituted by Al^{3+}, Ta^{5+}, and Al^{3+}+Ta^{5+} in the Ti sites, namely $CaCu_3Ti_{4-x}Ta_xO_{12+x/2}$ (x = 0.025, Ta025), $CaCu_3Ti_{4-x}Al_xO_{12-x/2}$ (x = 0.025, Al025), and $CaCu_3Ti_{4-x}(Ta_{1/2}Al_{1/2})_xO_{12}$. The starting raw materials used to synthesize the powders were Al_2O_3 (99.99%), Ta_2O_5 (99.99%), $CaCO_3$ (99.0%), and TiO_2 (99.99%), which were all purchased from Sigma Aldrich. CuO (99.9%) was purchased from Merck. Details of the preparation steps were comprehensively provided in the previous work [29]. The starting powders were weighed to give the desired nominal compositions, and the powder mixtures were calcined at 850 ℃ for 12 h. The ceramic samples were obtained by sintering in air at 1090 ℃ for 9 h using a 5 ℃/min heating rate. The sintered $CaCu_3Ti_{4-x}(Ta_{1/2}Al_{1/2})_xO_{12}$ samples with x = 0.05, 0.10, and 0.20 are henceforth abbreviated as TaAl05, TaAl10, and TaAl20, respectively.

Scanning electron microscopy (SEM; SNE-4500M), field-emission SEM (FE-SEM) with energy-dispersive X-ray spectroscopy (EDS; Hitachi SU8030), X-ray diffraction (XRD; PANalytical model Empyrean), and X-ray photoelectron spectroscopy (XPS; PHI5000

VersaProbe II, ULVAC-PHI) were used to characterize the sintered ceramics. The XRD patterns were analyzed using the X'Pert High Score Plus v3.0e software package with the Rietveld refinement technique, where the optimized structural parameters and coefficients were reported in the previous work [30]. Before SEM characterization, the top surface of the as-sintered samples was coated with Au using DC sputtering at 25 mA for 3 min.

To prepare the parallel electrodes for measuring the dielectric and electrical properties, the sample surfaces were polished until clean and smooth. The surfaces were then coated with Au in the same way as the SEM samples. The dielectric properties were measured using an E4990A impedance analyzer (Keysight Technology) with an oscillation voltage of 0.5 V over frequency and temperature ranges of 10^2–10^7 Hz and (−60)–210 ℃, respectively. The *J*–*E* field characteristics were tested at ~25 ℃ (Keithley model 247). The breakdown electric field (E_b) was obtained at J = 1 mA/cm^2. The nonlinear coefficient (α) was calculated over the J range of 1–10 mA/cm^2.

Density functional theory calculations were used to calculate the most preferential configuration for the Al and Ta dopants occupying the Ti sites of the $CaCu_3Ti_4O_{12}$ structure. The calculation details are described in the previous work [31]. The 3s and 3p valence states were chosen for the Al pseudopotential. For Ta, the 5p, 6s, and 5d states were used. In the current research, the unit cell of the $CaCu_3Ti_4O_{12}$ structure with 40 atoms was used.

3 Results

The XRD patterns of all samples are shown in Fig. 1(a). The XRD peaks of all samples corresponded to the characteristic peaks of the main CCTO phase (JCPDS No. 75-2188), with a body-centered cubic (bcc) structure with a space group of *Im*3 [32]. All samples showed the presence of only CCTO, with no remaining unreacted precursor materials or secondary phases. The Rietveld refinement method was successfully used to analyze the XRD patterns, where the pattern for the TaAl20 ceramic is shown in Fig. 1(b) as a representative example. The obtained results are summarized in Table 1. The *R*-factors (R_{exp}, R_p, and R_{wt}) obtained by Rietveld refinement were ~3.4%–6.1%, and the goodness of fit values were ~1.1–1.5. By considering the local environment of the metal ion M (reference coordinates: 0.25, 0.25, 0.25), where M = Ti, Al, or Ta, the bond lengths M–O and M–Cu of the (Al^{3+}, Ta^{5+})–CCTO ceramics were the same as those in the undoped CCTO ceramic. Furthermore, the bond angles (i.e., O–M–O, O–Cu–O, and Cu–M–Cu) in the CCTO structure either did not change after co-doping with Al^{3+} and Ta^{5+}. The *a* values of the Al025 and Ta025 ceramics were smaller and larger than that of the undoped CCTO ceramic, respectively, with the *a* values of the co-doped TaAl05, TaAl10, and TaAl20 ceramics between these extremes. The *a* values of all samples were similar to those presented in other studies [5,27,32].

The SEM images of the surface morphologies of all samples are shown in Fig. 2. The mean grain size (G) values of all samples are summarized in Table 1. Doping CCTO ceramics with Al^{3+} and/or Ta^{5+} greatly affected the microstructure. Compared with the pure CCTO ceramic, the G of Al025 was higher after partial substitution with Al^{3+}, while doping with Ta^{5+} resulted in a decrease in G. The changes in the G values of the Al^{3+} and Ta^{5+} single-doped CCTO ceramics were similar to those observed previously [5,33]. In addition, our findings are similar to the experimental results for the $CaCu_3Ti_{3.95}(Nb_{0.5}Al_{0.5})_{0.05}O_{12}$ ceramic [5]. However, the G of the TaAl10 and TaAl20 ceramics were much smaller than that of the Ta025 ceramic.

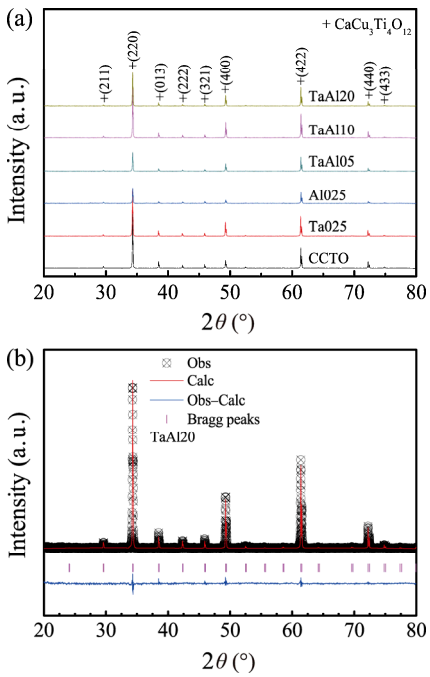

Fig. 1 (a) XRD patterns of the CCTO, Al025, Ta025, TaAl05, TaAl10, and TaAl20 ceramics. (b) Rietveld profile of TaAl20.

Table 1 Lattice parameter and structural data obtained from the Rietveld refinement, and the calculated grain size and relative density of the CCTO, Al025, Ta025, TaAl05, TaAl10, and TaAl20 ceramics

Sample	CCTO	Ta025	Al025	TaAl05	TaAl10	TaAl20
a (Å)	7.394(4)	7.395(5)	7.390(3)	7.393(0)	7.393(0)	7.393(9)
R_{exp} (%)	5.280(8)	4.156(0)	4.306(6)	4.284(5)	4.127(5)	4.214(1)
R_p (%)	3.818(1)	3.499(2)	3.639(5)	3.767(2)	3.524(1)	3.489(5)
R_{wp} (%)	6.182(8)	5.006(1)	5.007(4)	5.201(2)	4.824(4)	4.501(7)
GOF	1.370(8)	1.450(9)	1.352(0)	1.473(7)	1.366(2)	1.141(1)
Bond length (Å)	(M = Ta, Al, Ti)					
M–O	1.959(0)	1.959(0)	1.958(0)	1.959(0)	1.959(0)	1.959(0)
M–Cu	3.202(0)	3.202(0)	3.200(0)	3.201(0)	3.201(0)	3.202(0)
Bond angle (°)						
O–M–O	89.422(4)	89.422(4)	89.422(1)	89.422(1)	89.422(4)	89.422(4)
O–Cu–O	116.693(2)	116.693(0)	116.693(2)	116.693(2)	116.693(2)	116.693(1)
Cu–M–Cu	109.471(2)	109.471(2)	109.471(1)	109.471(1)	109.471(2)	109.471(2)
G (μm)	67.3 ± 21.9	15.9 ± 4.1	127.1 ± 39.3	25.3 ± 7.7	5.2 ± 1.2	3.8 ± 0.8
ρ (%)	94.60	94.58	94.20	93.57	96.46	94.52

a: lattice parameter; R_{exp}: expected residual; R_p: profile residual; R_{wp}: weighted profile residual; GOF: goodness of fit; G: mean grain size; ρ: relative density.

In addition, the apparent density values of all samples were measured using the Archimedes method. The relative densities of the sintered ceramics were calculated by dividing the apparent density by the theoretical density, as shown in Table 1. The relative densities of all samples were above 94%. Hence, sintering at 1090 ℃ for 9 h was considered acceptable for obtaining sufficiently dense ceramics.

The elemental distribution in all samples was evaluated using EDS mapping, as shown in Fig. 3. The distributions of Ca, Cu, Ti, Ta, and Al were very homogeneous for the TaAl20 ceramic. According to the XRD and EDS results, it is reasonable to conclude that the Ta and Al dopants were substituted well into the CCTO lattice.

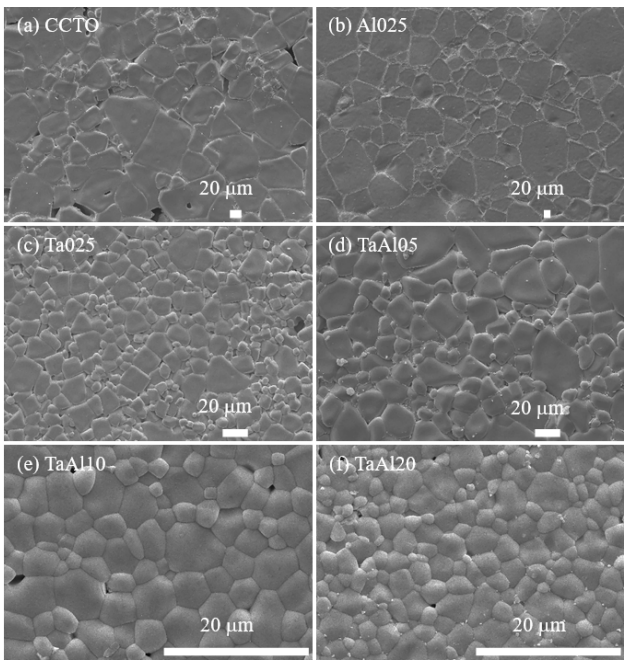

Fig. 2 SEM images of the surface morphologies of (a) CCTO, (b) Al025, (c) Ta025, (d) TaAl05, (e) TaAl10, and (f) TaAl20 ceramics.

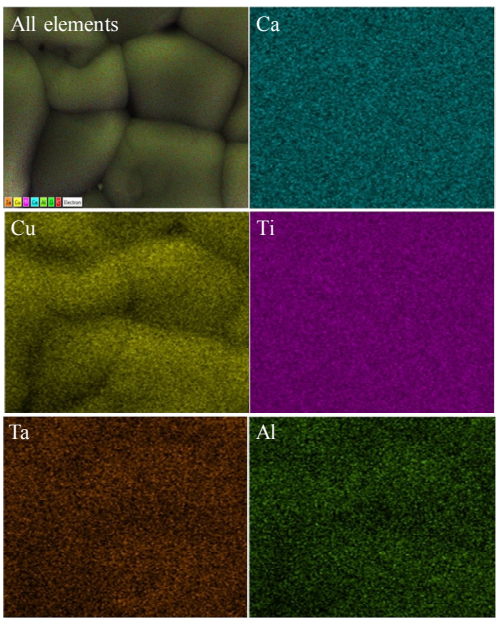

Fig. 3 EDS maps of TaAl20.

Figure 4(a) and its inset show the frequency-dependent ε' and tanδ of the undoped CCTO, and single-doped Al025 and Ta025 ceramics. The low-frequency ε' values of both Al025 and Ta025 were larger than that of the CCTO ceramic. The ε' values of the single-doped samples were frequency-dependent in the low-frequency range (10^2–10^3 Hz). As shown in the inset of Fig. 4(a), the low-frequency tanδ values of both Al025 and Ta025 were higher than that of pure CCTO. The ε' and tanδ values at 1 kHz of the CCTO, Al025, and Ta025 ceramics are summarized in Table 2, and showed that GDPs can be achieved with these three ceramics ($\varepsilon' > 10^4$). Nevertheless, the tanδ values are still too high for practical applications [34].

The frequency dependence of ε' and tanδ of the co-doped TaAl05, TaAl10, and TaAl20 ceramics measured at 20 ℃ are shown in Fig. 4(b). Interestingly, their ε' values showed a wider range of frequency stability than those of the undoped and single-doped samples. Furthermore, over the measured frequency range, the tanδ values of the co-doped CCTO ceramics were much lower than those of the undoped and single-doped samples. Significantly, the tanδ values in the low-frequency range (< 10^3 Hz) of the co-doped CCTO ceramics were low, indicating their improved dielectric properties, similar to the results of (Al^{3+}, Nb^{5+}) co-doped CCTO [5]. The ε' and tanδ values at 1 kHz for TaAl05, TaAl10, and TaAl20 are also listed in Table 2. Notably, large ε' values of ~(0.52–2.7) × 10^4 and very low tanδ values of ~0.010–0.036 were obtained with the co-doped CCTO ceramics. The high-performance dielectric properties of (Al^{3+}, Ta^{5+}) co-doped CCTO ceramics may be the first step to improve their properties sufficiently for use in capacitor applications.

In addition to their high ε' and very low tanδ values, Fig. 5 shows that the ε' values of the (Al^{3+}, Ta^{5+}) co-doped CCTO ceramics were much less temperature dependent than the pure and single-doped CCTO ceramics. The greatly improved thermal stability of ε' could be associated with the enhanced GB response as a result of co-doping. Interestingly, the variations in ε' of the TaAl10 and TaAl20 ceramics are consistent with the required standards for capacitor applications [34]. The improved temperature stability of ε' for the co-doped CCTO ceramics is consistent with that reported for co-doped TiO_2, and single- and co-doped CCTO ceramics [4,5,28,35,36].

In general, the ε' values of the undoped and doped CCTO ceramics are considered high. Therefore, the origin of the GDPs in this material may differ from that

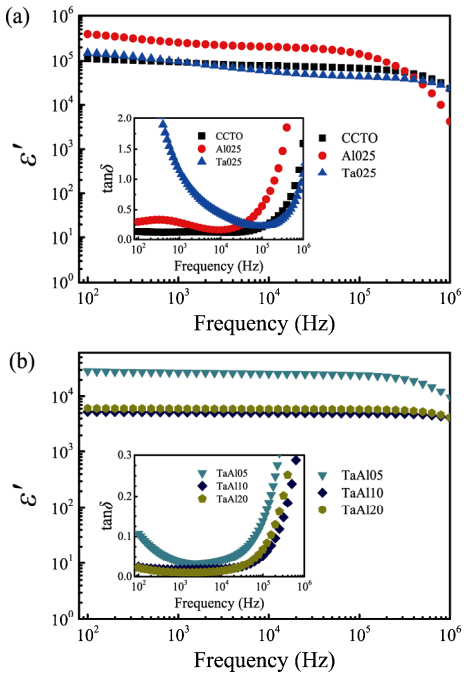

Fig. 4 (a) Frequency-dependence of ε' for CCTO, Al025, and Ta025 at 20 ℃. Inset: frequency-dependence of tanδ. (b) Frequency-dependence of ε' for the TaAl05, TaAl10, and TaAl20 ceramics at 20 ℃. Inset: frequency-dependence of tanδ.

Table 2 ε' **and tanδ values measured at 1 kHz and 20 ℃, grain resistance (R_g) at 20 ℃, grain boundary resistance (R_{gb}) at 110 ℃, conduction activation energies of the grain (E_g) and grain boundary (E_{gb}), breakdown electric field (E_b), and nonlinear coefficient (α) of the CCTO, Al025, Ta025, TaAl05, TaAl10, and TaAl20 ceramics**

Sample	ε'	tanδ	R_g (Ω·cm)	R_{gb} (Ω·cm)	E_g (eV)	E_{gb} (eV)	E_b (V·cm^{-1})	α
CCTO	9.15×10^4	0.121	33	5.08×10^4	0.086	0.682	200.71	4.82
Al025	2.55×10^5	0.289	46	5.96×10^3	0.111	0.656	77.09	4.75
Ta025	9.44×10^4	1.147	37	4.06×10^2	0.091	0.416	22.50	2.24
TaAl05	2.70×10^4	0.036	82	8.49×10^4	0.095	0.732	491.57	5.19
TaAl10	5.15×10^3	0.017	145	1.81×10^6	0.094	0.724	497.87	2.86
TaAl20	5.98×10^3	0.010	170	1.31×10^6	0.097	0.713	6588.38	15.20

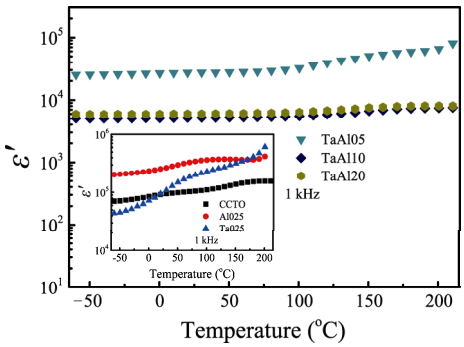

Fig. 5 Temperature dependence of ε' at 1 kHz of TaAl05, TaAl10, and TaAl20. Inset: temperature dependence of ε' at 1 kHz of CCTO, Al025, and Ta025.

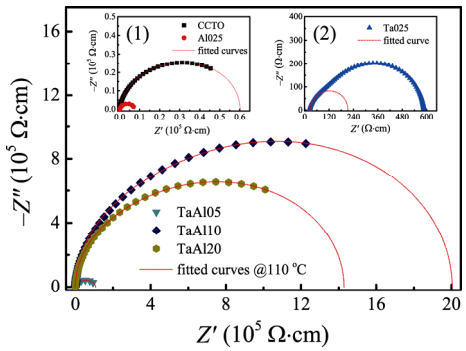

Fig. 6 Complex impedance (Z^*) plots measured at 110 ℃ for TaAl05, TaAl10, and TaAl20. Insets: Z^* plots of (1) CCTO and Al025, and (2) Ta025.

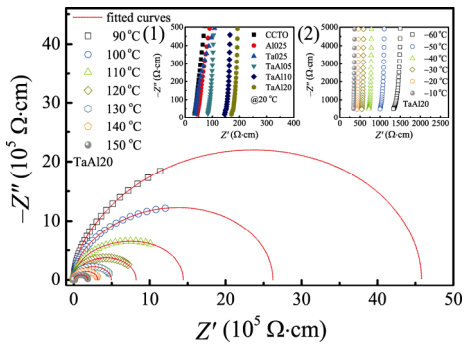

Fig. 7 Complex impedance (Z^*) plots measured at high temperature for TaAl20. Insets: high-frequency Z^* plots of (1) CCTO, Al025, Ta025, TaAl05, TaAl10, and TaAl20, and (2) TaAl20 at low temperature (−60 to −10 ℃).

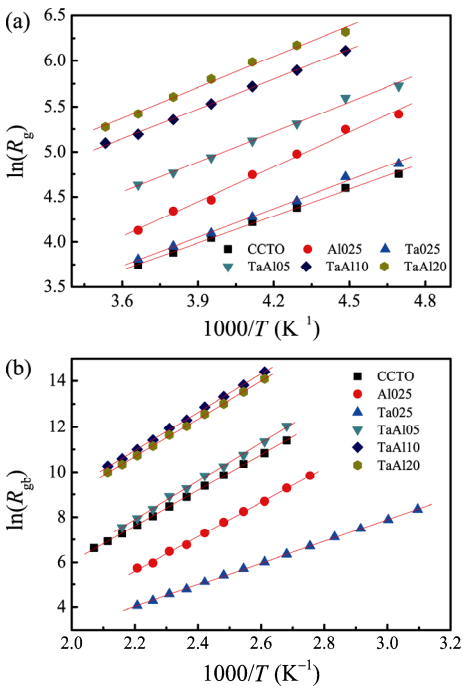

Fig. 8 Arrhenius plots of (a) R_g and (b) R_{gb} for CCTO, Al025, Ta025, TaAl05, TaAl10, and TaAl20.

of co-doped TiO_2 ceramics [4,17]. Furthermore, doping CCTO with only Ta^{5+} or Al^{3+} cannot enhance the dielectric properties above those of undoped and co-doped CCTO. Thus, the reduction of tanδ is attributed to the synergistic effect of the Al^{3+} and Ta^{5+} dopants.

Impedance spectroscopy was used to clarify the possible mechanisms of the GDPs in each ceramic. The resistance of the grain (R_g) and GB (R_{gb}) was estimated from the nonzero intercept at high frequency and the semicircular arc of the complex impedance (Z^*) plot, respectively [37]. Heterogeneous ceramic components consisting of semiconducting grains and insulating GBs were identified for all of the prepared ceramics [5,37], as shown in Figs. 6 and 7. As shown in Fig. 6, the R_{gb} values of the co-doped CCTO ceramics were much larger than those of CCTO, Al025 (inset (1) of Fig. 6), and Ta025 (inset (2) of Fig. 6). The R_g values at 20 ℃ of all the co-doped CCTO ceramics were also larger than those of the undoped and single-doped CCTO ceramics, as shown in the inset (1) of Fig. 7 and listed in Table 2. The variations in the R_{gb} and R_g values of the TaAl20 ceramic at different temperatures are shown in Fig. 7 and its inset (2). As shown in these two figures, the R_{gb} and R_g values decreased significantly with even small increase in temperature. The trends in the R_{gb} and R_g values at different temperatures are consistent with the characteristic dielectric behavior observed for CCTO and its related structures [2,5,21,33,37]. As shown in Figs. 8(a) and 8(b), the temperature dependence of R_g and R_{gb} followed the Arrhenius law well. The conduction activation energies of the grains (E_g) and GBs (E_{gb}) were calculated from the slopes of the lines of best fit, and are listed in Table 2. The obtained E_g values of the ceramics were all slightly different, while the E_{gb} values of the co-doped CCTO ceramics were significantly larger than those of undoped and

single-doped CCTO ceramics.

Nonlinear *J–E* properties were observed for all samples, as shown in Fig. 9. The E_b values of all co-doped CCTO ceramics were significantly larger than those of undoped and single-doped CCTO ceramics. Furthermore, E_b significantly increased with increasing dopant content. The lowest E_b value was measured for the single-doped Ta025 ceramic. Among the samples analyzed in this study, the best nonlinear *J–E* properties, with an E_b of ~6.59 × 10^3 V·cm^{-1} and α of ~15.20, were measured for the TaAl20 ceramic. The improved nonlinear *J–E* properties imparted by co-doping was consistent with previous results for (Al^{3+}, Nb^{5+}), (Zn^{2+}, Mn^{4+}), and (Y^{3+}, Zr^{4+}) co-doped CCTO ceramics [5,12,35]. According the dielectric and nonlinear results, it can be considered that the primary benefits of the (Al^{3+}, Ta^{5+}) co-doped CCTO ceramics are their reduced tanδ and improved nonlinear properties. The dielectric and nonlinear electrical properties of the TaAl20 ceramic were compared to those of other co-doped CCTO ceramics with various pairs of ions co-substituting the B-site Ti^{4+}, as summarized in Table 3. TaAl20 showed the best overall performance of all CCTO ceramics, with the lowest tanδ value and the highest E_b and α values.

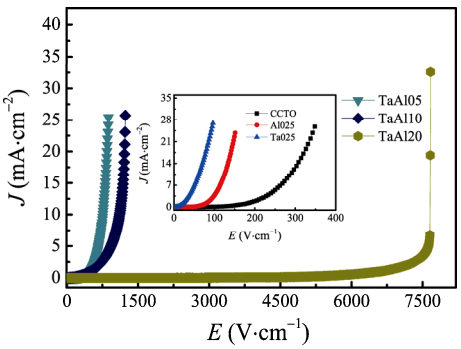

Fig. 9 Nonlinear *J–E* properties of TaAl05, TaAl10, and TaAl20 and inset of CCTO, Al025, and Ta025.

The valence structures and charge compensation mechanisms for the CCTO, TaAl10, and TaAl20 ceramics were systematically investigated using XPS. As shown in Figs. 10(a)–10(c), Gaussian–Lorentzian profile fitting was used to reproduce the $Cu2p_{3/2}$ peaks for the CCTO, TaAl10, and TaAl20 ceramics. The asymmetric shape of the $Cu2p_{3/2}$ peaks indicates several overlapping peaks, i.e., the presence of both smaller Cu^+ and larger Cu^{2+} peaks. The smaller peak of Cu^+ was observed at a binding energy (BE) of ~931.85–932.30 eV, while the larger peak of Cu^{2+} was detected at ~933.99–934.33 eV. The ratios between Cu^+/Cu^{2+} for the CCTO, TaAl10, and TaAl20 ceramics were 15.47%/84.53%, 14.19%/85.81%, and 12.69%/87.31%, respectively.

The XPS spectra of Ti2p for the CCTO, TaAl10, and TaAl20 ceramics are shown in Figs. 10(d)–10(f). Smaller and larger peaks in the $Ti2p_{3/2}$ spectra were detected at BE positions of ~457.10–457.23 eV and ~458.07–458.30 eV, respectively, corresponding to Ti^{3+} and Ti^{4+}, respectively. The ratios between Ti^{3+}/Ti^{4+} of CCTO, TaAl10, and TaAl20 ceramics were 6.91%/93.39%, 5.16%/94.84%, and 4.65%/95.35%, respectively. The presence of Cu^+ and Ti^{3+} is consistent with previous reports [5,33,38].

To investigate the possible configurations of the defect structures in the (Al^{3+}, Ta^{5+}) co-doped CCTO ceramics, first-principles calculations were performed. Two initial defect configurations were set up, as shown in Fig. 11. We first created structure I by replacing two Ti ions with Al and Ta ions in the CCTO structure; however, Al and Ta ions in the octahedral sites were placed far apart. The total energy of structure I was

Table 3 Comparison of the dielectric properties (at 1 kHz and ~25℃) and nonlinear properties of (Al^{3+}, Ta^{5+})–CCTO ceramics with other CCTO ceramics with other ion pairs co-substituted for the B-site Ti^{4+}

Sample	ε'	tanδ	E_b (V/cm)	α	Ref.
$CaCu_3Ti_{3.95}(Nb_{0.025}Al_{0.025})O_{12}$	2.90 × 10^4	0.045	~0.72 × 10^3	~5.76	[5]
$CaCu_3Ti_{3.992}(Nb_{0.004}Al_{0.004})O_{12}$	~3.00 × 10^4	< 0.49	—	—	[6]
$CaCu_3Ti_{3.975}(Nb_{0.0125}In_{0.0125})O_{12}$	~4.54 × 10^4	~0.266	—	—	[7]
$CaCu_3Ti_{3.975}(Ta_{0.0125}In_{0.0125})O_{12}$	3.86 × 10^4	0.075	—	—	[8]
$CaCu_3Ti_4O_{12}$(0.5%Ta/0.5% In)	2.36 × 10^3	0.024	~9.67 × 10^3	~6.69	[9]
$CaCu_3Ti_{3.00}Nb_{0.20}Zr_{0.80}O_{12}$	~10^3	~0.2	—	—	[10]
$CaCu_3Ti_{3.74}Zr_{0.06}Nb_{0.2}O_{12}$	2.0 × 10^5	~0.23	—	—	[11]
$CaCu_3Ti_{3.92}Y_{0.03}Zr_{0.05}O_{11.985}$	~1.15 × 10^4	~0.05	~1.21 × 10^3	~4.5	[12]
$CaCu_3(Ti_{0.50}Fe_{0.25}Nb_{0.25})_4O_{12}$	~10^5	~1.2	~35	~2.27	[13]
$CaCu_3Ti_{3.8}(Ta_{1/2}Al_{1/2})_{0.2}O_{12}$ (TaAl20)	5.98 × 10^3	0.010	~6.6 × 10^3	15.20	This work

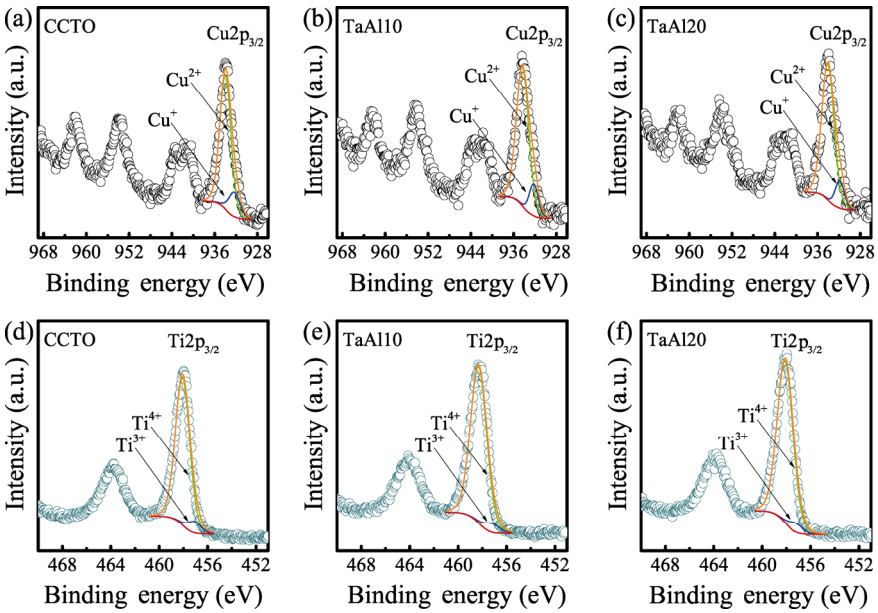

Fig. 10 (a–c) Cu2p XPS spectra and (e–h) Ti2p spectra of CCTO, TaAl10, and TaAl20, respectively.

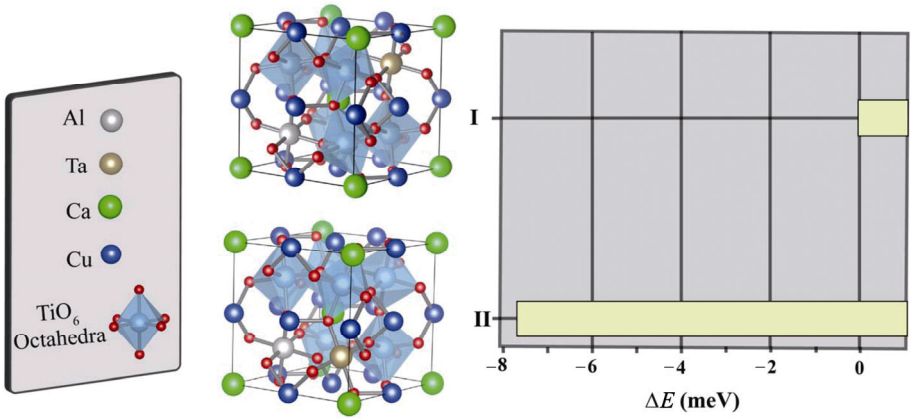

Fig. 11 Total energy of Al and Ta co-doped CCTO structure when (1) Al atom is far from Ta atom (structure I) and (2) Al and Ta atoms are close to each other (structure II).

then calculated. Then, the total energy was calculated for structure II with the two Al and Ta dopant ions in adjacent octahedral sites. Figure 11 clearly shows that the total energy of structure II is lower than that of structure I by 7.68 meV. Hence, the Al and Ta dopants in the CCTO host prefer to be in proximity. Generally, the substitution of Ta^{5+} for Ti^{4+} requires charge compensation by the formation of free electrons according to the following relations.

$$2TiO_2 + Ta_2O_5 \xrightarrow{4TiO_2} 2Ti'_{Ti} + 2Ta^{\bullet}_{Ti} + 8O_O + \frac{1}{2}O_2 \quad (1)$$

$$Ti^{4+} + e \rightarrow Ti^{3+} \quad (2)$$

In contrast, the substitution of Ti^{4+} with Al^{3+} requires the formation of oxygen vacancies ($V_O^{\bullet\bullet}$) for charge compensation, according to the relation:

$$Al_2O_3 \xrightarrow{2TiO_2} 2Al'_{Ti} + V_O^{\bullet\bullet} + 3V_O \quad (3)$$

In the case of structure II, when the two octahedral sites of the CCTO structure containing the Al and Ta dopants are close together, there is no need for charge compensation, as shown by the following relation:

$$Al_2O_3 + Ta_2O_5 \xrightarrow{4TiO_2} 2Al'_{Ti} + 2Ta^{\bullet}_{Ti} + 8O_O \quad (4)$$

Consequently, self-charge compensation between these two ions occurs in our structure without the formation of free electrons or oxygen vacancies.

4 Discussion

4. 1 Structure and phase formation

Changes in the *a* values of both the single- and co-doped ceramics were consistent with the differences between the ionic radii of Al^{3+} (r_6 = 0.535 Å) and Ta^{5+} (r_6 = 0.72 Å) doping ions and Ti^{4+} (r_6 = 0.605 Å) host sites [39]. Variations in the *a* values of the Al025 and Ta025 ceramics compared to that of the CCTO ceramic were caused by the different ionic radii between the dopant and host ions. The ionic radii of all co-doped ceramics were slightly smaller than that of the CCTO ceramic because the average ionic radius of the co-dopants (0.588 Å) was slightly smaller than that of Ti^{4+}. The same *a* for the TaAl05 and TaAl10 ceramics and slightly higher *a* of TaAl20 were because of the average ionic radius of the co-dopants being similar to that of Ti^{4+}.

4. 2 Microstructural evolution

Generally, the grain growth in polycrystalline ceramics is associated with GB mobility (M_b), which is dependent on the diffusion of ions, atoms, and/or charged species across the GB [40]. It was previously shown that the grain-growth and densification rates of CCTO ceramics were lower when sintering in an oxidizing atmosphere than a reducing atmosphere [41]. Thus, the diffusion of oxygen ions (O^{2-}), which is directly dependent on the $V_O^{\bullet\bullet}$ concentration, is an important factor influencing the higher grain-growth rate. According to Eq. (3), the large increase in *G* for the single-doped Al025 ceramic (~127 μm) compared to that of the CCTO ceramic (~67.3 μm) was likely associated with the higher diffusion coefficient of O^{2-} due to the increase in $V_O^{\bullet\bullet}$ as a result of the partial substitution of Al^{3+} on Ti^{4+} sites. This could also be attributed to the presence of liquid-phase sintering. The eutectic liquid in CCTO ceramics can be formed above 919 ℃, facilitating the diffusion of ions across the GBs [42].

In contrast, the smaller *G* of the single-doped Ta025 ceramic (~15.9 μm) compared to the Al025 ceramic was because of Ta^{5+} ions inhibiting the grain growth, as demonstrated previously for CCTO-based ceramics [33]. According to Eq. (1), the grain growth of the Ta025 ceramic was not increased by the increased diffusivity of O^{2-}, resulting in a relatively low grain-growth rate compared to that of Al025. Furthermore, the *G* value of Ta025 was much smaller than that of CCTO. Similarly, the decrease in *G* of $BaTiO_3$ ceramics doped with Nb^{5+} (> 0.5 at%) was explained based on the space-charge and defect-chemistry concepts [43]. The R_g of Ta025 was slightly larger than that of CCTO, which does not obey Eq. (1), and is instead explained by Eq. (5), where most of the Ta^{5+} ions are ionically compensated by cation vacancies (V_{Ti}'''').

$$2Ta_2O_5 + 3TiO_2 \xrightarrow{8TiO_2} 4Ta_{Ti}^{\bullet} + V_{Ti}'''' + 3Ti_{Ti}^{\times} + 16O_O^{\times} \quad (5)$$

In this case, V_{Ti}'''' and electrons were expected to accumulate in the negative space-charge region [44]. The accumulated V_{Ti}'''' are likely related to a depletion of the oxygen vacancies in the space-charge region, where the diffusivity of O^{2-} across the GB was slow because of the large ionic size of O^{2-}. This resulted in the reduction of M_b, which was a possible reason for the significantly reduced *G* value of Ta025 compared to that of CCTO. According to the first-principles calculations and Eq. (4), the decrease in *G* of the co-doped TaAl10 and TaAl20 ceramics with increasing the doping content was because of self-charge compensation between Al^{3+} and Ta^{5+} on the Ti^{4+} sites. The *G* values of the co-doped TaAl10 and TaAl20 ceramics were between those of the single-doped Al025 and Ta025 ceramics, indicating the balance between driving and inhibiting forces for GB migration. Thus, the charge compensation by the formation of oxygen vacancies did not occur in these materials. Furthermore, the Cu-rich phase was not observed for TaAl10 and TaAl20, as confirmed by EDS maps (Fig. 3).

4. 3 Origins of the GDPs and enhanced grain and GB properties

The strong frequency dependence of the low-frequency ε' for the Al025 ceramic (Fig. 4(a)) was considered to originate from the dielectric response of the sample–electrode interface [5]. This result is consistent with the appearance of a low-frequency dielectric relaxation peak in the $\tan\delta$ curve (10^2–10^3 Hz) (inset of Fig. 4(a)). These results clearly indicate the additional dielectric response from the sample–electrode interface, which was dominant when the R_{gb} of the Al025 ceramic significantly decreased from 5.08×10^4 to 5.96×10^3 Ω·cm at 110 ℃ [45,46]. Furthermore, the ε' of Ta025 was frequency independent over a wide range of frequencies, while the low-frequency $\tan\delta$ significantly increased with decreasing frequency from 10^5 to 10^2 Hz. A shoulder of the $\tan\delta$ peak was observed at 10^3–10^4 Hz, indicating

a hidden peak. The strong increase in tanδ below 10^2 Hz was because of the long-range migration of charges or DC conduction in Ta025 [5,33], corresponding to its lowest R_{gb} value (4.06×10^2 Ω·cm).

According to the IBLC structure [19], a simple series layer model can be developed for explaining the giant dielectric response: $\varepsilon' = \varepsilon_{gb}G/t_{gb}$, where ε_{gb} and t_{gb} are the dielectric constant and thickness of the GB, respectively. Thus, the lower ε' values of all of the (Al^{3+}, Ta^{5+})–CCTO ceramics than that of pure CCTO were because of their lower G values. In contrast, the much higher ε' value of the Al025 ceramic was attributed to its high G value. However, the ε' of Ta025 was slightly higher than that of CCTO, even though its G value was much smaller. In addition to the mean G, the ε' was also determined from ε_{gb}, which is associated with the GB capacitance (C_{gb}). The C_{gb} per unit GB area, which was equal to G, can be expressed as [37]:

$$C_{gb} / G = \left(\frac{\varepsilon' q N_d}{8\Phi_b} \right)^{1/2} \quad (6)$$

Here, C_{gb}/G is inversely proportional to Φ_b, which was clearly shown to be closely correlated with the E_{gb} value ($C_{gb}/G \propto 1/E_{gb}$). Although C_{gb}/G is proportional to the charge carrier concentration inside the semiconducting grains (N_d) or inversely proportional to R_g, the different R_g values of the CCTO and Ta025 ceramics are too small. As shown in Table 2, the E_{gb} value of Ta025 was the lowest of all samples (0.416 eV), giving rise to the largest C_{gb}/G, and hence, highest ε' value.

According to impedance spectroscopy results, the improved dielectric properties observed for the co-doped ceramics may have been a result of a greatly enhanced GB response [5]. The increases in R_{gb} and E_{gb} in the co-doped CCTO ceramics originated from the reduction in G and improved electrical properties of the GBs owing to co-doping. The low-frequency tanδ of the co-doped ceramics was closely related to their large R_{gb} and E_{gb} [5,27]. Due to the IBLC structure, $R_g << R_{gb}$, where the correlation between tanδ in the low-frequency range and R_{gb} is described as follows:

$$\tan\delta \approx \frac{1}{w\varepsilon_0\varepsilon_s' C_0 R_{gb}} \quad (7)$$

where ε'_s is the dielectric constant in the low-frequency range, and $C_0 = \varepsilon_0 A/t$ is the free space capacitance, where A and t are the area of electrodes and the sample thickness, respectively. The lower tanδ values of the (Al^{3+}, Ta^{5+})–CCTO ceramics at low frequencies, which was compared to the undoped, observed here are consistent with Eq. (7), where tanδ is associated with DC conductivity ($\sigma_{dc} \propto 1/R_{gb}$). As shown in the inset of Fig. 4(b), the tanδ values at 10^2 Hz of TaAl10 and TaAl20 were significantly lower than that of TaAl05. This was attributed to the remarkable decrease in σ_{dc}, observed by the significant increase in R_{gb}, which resulted in the long-range motion of free charge carriers being completely inhibited by the GBs with very high resistance and Φ_b. Note that, the lower R_{gb} of the single-doped Al025 and Ta025 ceramics compared to CCTO, which resulted in the higher tanδ value, was similar to the behavior reported for Nb^{5+} and Ta^{5+} single-doped CCTO ceramics [5,33,47,48]. The improved temperature dependence of the ε' of the co-doped ceramics was because of the high R_{gb}.

The different E_b values measured for the ceramic samples evaluated here may be because of differences in their microstructure and the electrical properties of the GBs. The higher α values measured for TaAl20 may have been a result of the high E_{gb} and R_{gb} that indicate a high Φ_b at the GBs that the charges need to overcome [49]. Several previous studies reported that α simultaneously increases with E_b [5,29,49–51]. For such ceramics, $E_b = N_{gb}E_{b,gb} = (tE_{b,gb})/G$, where N_{gb} is the number of GBs and $E_{b,gb}$ is the breakdown field of an individual GB layer. Therefore, the macroscopically enhanced E_b value of the (Al^{3+}, Ta^{5+})–CCTO ceramics should be primarily correlated to the microstructure because of a significant decrease in G (or significant increase in N_{gb}). The low E_b value of Al025 was its high G value, while the lowest E_b value of Ta025 (despite its small G value) was a result of its lowest Φ_b.

The XPS results showed the presence of Cu^+ and Ti^{3+} ions, which may have been formed as a charge-compensation mechanism due to oxygen loss during sintering, following the relationship:

$$2O_O^{\times} \rightarrow O_2 + V_O^{\bullet\bullet} + 2e' \quad (8)$$

corresponding to the formation of the IBLC structure [52]. This gave rise to the presence of Cu^+ and Ti^{3+}, as shown in Eq. (2) and $Cu^{2+} + e \rightarrow Cu^+$. Interestingly, an increase in R_g is highly consistent with a decrease in the concentration of Cu^+ and Ti^{3+} in the sintered samples. It is reasonable to suggest that co-substitution of Ta^{5+} and Al^{3+} can suppress oxygen loss during sintering at high temperature. When the co-dopants were close together in the CCTO structure, fewer $V_O^{\bullet\bullet}$ defects

tended to form, resulting in a decrease in the Cu^{+}/Cu^{2+} and Ti^{3+}/Ti^{4+} ratios. According to the first-principles calculations (Fig. 11), self-charge compensation between Al^{3+} and Ta^{5+} ions probably occurred, which prevented the formation of further $V_O^{\bullet\bullet}$ and enhanced free charge carriers. Therefore, co-doping can result in an increase in R_{gb} and R_g, which greatly decreases tanδ.

5 Conclusions

In conclusion, we confirmed that acceptor–donor co-doping of CCTO ceramics to reduce tanδ and improve the nonlinear properties is also effective for (Al^{3+}, Ta^{5+}) dopants, where wide regions of frequency- and temperature-independent dielectric properties were observed. The substitution of (Al^{3+}, Ta^{5+}) dopants into the TiO_6 octahedral sites of the CCTO ceramics greatly reduced tanδ, compared to the single-doped counterparts, indicating the synergistic effect of the dopants. The nonlinear *J*–*E* properties of the (Al^{3+}, Ta^{5+}) co-doped CCTO ceramics were also greatly improved and attributed to the enhanced electrical properties of the GBs, which were well described by the IBLC model. Although the tanδ values are quite high for practical applications, our results further strengthen the argument for acceptor–donor co-doping of CCTO ceramics for producing electroceramics with excellent GDPs.

Acknowledgements

This work was supported by the Basic Research Fund of Khon Kaen University. It was partially supported by the Research Network NANOTEC (RNN) program of the National Nanotechnology Center (NANOTEC), NSTDA, Ministry of Higher Education, Science, Research, and Innovation (MHESI, Thailand) (Grant No. P1851882), and Khon Kaen University, Thailand. J. Boonlakhorn would like to thank the Graduate School of Khon Kaen University (Grant No. 581T211) for his Ph.D. scholarship.

References

[1] Guo BC, Liu P, Cui X, *et al*. Enhancement of breakdown electric field and DC bias of $(In_{0.5}Nb_{0.5})_{0.005}(Ti_{1-x}Zr_x)_{0.995}O_2$ colossal permittivity ceramics. *J Alloys Compd* 2018, **740**: 1108–1115.

[2] Liang P, Wang X, Chao X, *et al*. Electric response and improved dielectric properties in $BiCu_3Ti_3FeO_{12}$. *J Alloys Compd* 2018, **734**: 9–15.

[3] Wang XW, Jia PB, Sun LY, *et al*. Improved dielectric properties in $CaCu_3Ti_4O_{12}$ ceramics modified by TiO_2. *J Mater Sci*: *Mater Electron* 2018, **29**: 2244–2250.

[4] Hu W, Liu Y, Withers RL, *et al*. Electron-pinned defect-dipoles for high-performance colossal permittivity materials. *Nat Mater* 2013, **12**: 821–826.

[5] Boonlakhorn J, Kidkhunthod P, Chanlek N, *et al*. (Al^{3+}, Nb^{5+}) co-doped $CaCu_3Ti_4O_{12}$: An extended approach for acceptor-donor heteroatomic substitutions to achieve high-performance giant-dielectric permittivity. *J Eur Ceram Soc* 2018, **38**: 137–143.

[6] Wen A, Yuan D, Zhu X, *et al*. Electrical and dielectric properties of aluminum/niobium co-doped $CaCu_3Ti_4O_{12}$ ceramics. *Ferroelectrics* 2016, **492**: 1–9.

[7] Boonlakhorn J, Kidkhunthod P, Thongbai P. Effects of co-doping on dielectric and electrical responses of $CaCu_3Ti_{4-x}(Nb_{1/2}In_{1/2})_xO_{12}$ ceramics. *J Phys*: *Conf Ser* 2017, **901**: 012078.

[8] Boonlakhorn J, Srepusharawoot P, Thongbai P. Distinct roles between complex defect clusters and insulating grain boundary on dielectric loss behaviors of (In^{3+}/Ta^{5+}) co-doped $CaCu_3Ti_4O_{12}$ ceramics. *Results Phys* 2020, **16**: 102886.

[9] Sun J, Xu C, Zhao X, *et al*. Improved dielectric properties of indium and tantalum co-doped $CaCu_3Ti_4O_{12}$ ceramic prepared by spark plasma sintering. *IEEE Trans Dielectr Electr Insul* 2020, **27**: 1400–1408.

[10] Hasan MK, Shant SH, Islam MZ, *et al*. Influence of Nb and Zr co-doping on the structural, morphological and dielectric properties of $CaCu_3Ti_4O_{12}$ ceramics. *IOP Conf Ser*: *Mater Sci Eng* 2021, **1045**: 012004.

[11] Mao P, Wang J, Xiao P, *et al*. Colossal dielectric response and relaxation behavior in novel system of Zr^{4+} and Nb^{5+} co-substituted $CaCu_3Ti_4O_{12}$ ceramics. *Ceram Int* 2021, **47**: 111–120.

[12] Xu Z, Qiang H, Chen Y, *et al*. Microstructure and enhanced dielectric properties of yttrium and zirconium co-doped $CaCu_3Ti_4O_{12}$ ceramics. *Mater Chem Phys* 2017, **191**: 1–5.

[13] Bai L, Wu Y, Zhang L. Influence of FeNb codoping on the dielectric and electrical properties of $CaCu_3Ti_4O_{12}$ ceramics. *J Alloys Compd* 2016, **661**: 6–13.

[14] Qu Y, Wu Y, Wu J, *et al*. Simultaneous epsilon-negative and mu-negative property of Ni/$CaCu_3Ti_4O_{12}$ metacomposites at radio-frequency region. *J Alloys Compd* 2020, **847**: 156526.

[15] Qu Y, Du Y, Fan G, *et al*. Low-temperature sintering Graphene/$CaCu_3Ti_4O_{12}$ nanocomposites with tunable negative permittivity. *J Alloys Compd* 2019, **771**: 699–710.

[16] Qu Y, Lin J, Wu J, *et al*. Graphene-carbon black/$CaCu_3Ti_4O_{12}$ ternary metacomposites toward a tunable and weakly ε-negative property at the radio-frequency region. *J Phys Chem C* 2020, **124**: 23361–23367.

[17] Hu W, Lau K, Liu Y, *et al*. Colossal dielectric permittivity in (Nb+Al) codoped rutile TiO_2 ceramics: Compositional

gradient and local structure. *Chem Mater* 2015, **27**: 4934–4942.

[18] Song Y, Wang X, Zhang X, *et al*. Colossal dielectric permittivity in (Al + Nb) co-doped rutile SnO_2 ceramics with low loss at room temperature. *Appl Phys Lett* 2016, **109**: 142903.

[19] Wu J, Nan CW, Lin Y, *et al*. Giant dielectric permittivity observed in Li and Ti doped NiO. *Phys Rev Lett* 2002, **89**: 217601.

[20] Peng Z, Liang P, Wang X, *et al*. Fabrication and characterization of $CdCu_3Ti_4O_{12}$ ceramics with colossal permittivity and low dielectric loss. *Mater Lett* 2018, **210**: 301–304.

[21] Jumpatam J, Somphan W, Boonlakhorn J, *et al*. Non-ohmic properties and electrical responses of grains and grain boundaries of $Na_{1/2}Y_{1/2}Cu_3Ti_4O_{12}$ ceramics. *J Am Ceram Soc* 2017, **100**: 157–166.

[22] Peng Z, Wu D, Liang P, *et al*. Grain boundary engineering that induces ultrahigh permittivity and decreased dielectric loss in $CdCu_3Ti_4O_{12}$ ceramics. *J Am Ceram Soc* 2020, **103**: 1230–1240.

[23] Peng Z, Liang P, Wang J, *et al*. Interfacial effect inducing thermal stability and dielectric response in $CdCu_3Ti_4O_{12}$ ceramics. *Solid State Ion* 2020, **348**: 115290.

[24] Winkler E, Rivadulla F, Zhou JS, *et al*. Evolution of polaron size in $La_{2-x}Sr_xNiO_4$. *Phys Rev B* 2002, **66**: 094418.

[25] Wang CC, Zhang LW. Surface-layer effect in $CaCu_3Ti_4O_{12}$. *Appl Phys Lett* 2006, **88**: 042906.

[26] Lunkenheimer P, Fichtl R, Ebbinghaus S, *et al*. Nonintrinsic origin of the colossal dielectric constants in $CaCu_3Ti_4O_{12}$. *Phys Rev B* 2004, **70**: 172102.

[27] Sun L, Zhang R, Wang Z, *et al*. Microstructure and enhanced dielectric response in Mg doped $CaCu_3Ti_4O_{12}$ ceramics. *J Alloys Compd* 2016, **663**: 345–350.

[28] Tuichai W, Thongyong N, Danwittayakul S, *et al*. Very low dielectric loss and giant dielectric response with excellent temperature stability of Ga^{3+} and Ta^{5+} co-doped rutile-TiO_2 ceramics. *Mater Des* 2017, **123**: 15–23.

[29] Boonlakhorn J, Kidkhunthod P, Thongbai P. A novel approach to achieve high dielectric permittivity and low loss tangent in $CaCu_3Ti_4O_{12}$ ceramics by co-doping with Sm^{3+} and Mg^{2+} ions. *J Eur Ceram Soc* 2015, **35**: 3521–3528.

[30] Silva Junior E, La Porta FA, Liu MS, *et al*. A relationship between structural and electronic order-disorder effects and optical properties in crystalline TiO_2 nanomaterials. *Dalton Trans* 2015, **44**: 3159–3175.

[31] Boonlakhorn J, Chanlek N, Thongbai P, *et al*. Strongly enhanced dielectric response and structural investigation of (Sr^{2+}, Ge^{4+}) co-doped CCTO ceramics. *J Phys Chem C* 2020, **124**: 20682–20692.

[32] Subramanian MA, Li D, Duan N, *et al*. High dielectric constant in $ACu_3Ti_4O_{12}$ and $ACu_3Ti_3FeO_{12}$ phases. *J Solid State Chem* 2000, **151**: 323–325.

[33] Thongbai P, Jumpatam J, Yamwong T, *et al*. Effects of Ta^{5+} doping on microstructure evolution, dielectric properties and electrical response in $CaCu_3Ti_4O_{12}$ ceramics. *J Eur Ceram Soc* 2012, **32**: 2423–2430.

[34] Moulson AJ, Herbert JM. *Electroceramics: Materials, Properties, Applications*, 2nd edn. New York; Wiley, 2003: 243–337

[35] Xu Z, Qiang H. Enhanced dielectric properties of Zn and Mn co-doped $CaCu_3Ti_4O_{12}$ ceramics. *J Mater Sci*: *Mater Electron* 2017, **28**: 376–380.

[36] Li M, Liu Q, Li CX. Study of the dielectric responses of Eu-doped $CaCu_3Ti_4O_{12}$. *J Alloys Compd* 2017, **699**: 278–282.

[37] Adams T, Sinclair D, West A. Characterization of grain boundary impedances in fine- and coarse-grained $CaCu_3Ti_4O_{12}$ ceramics. *Phys Rev B* 2006, **73**: 094124.

[38] Moreno H, Cortés JA, Praxedes FM, *et al*. Tunable photoluminescence of $CaCu_3Ti_4O_{12}$ based ceramics modified with tungsten. *J Alloys Compd* 2021, **850**: 156652.

[39] Shannon RD. Revised effective ionic radii and systematic studies of interatomic distances in halides and chalcogenides. *Acta Cryst Sect A* 1976, **32**: 751–767.

[40] Rahaman MN. *Ceramic Processing and Sintering*, 2nd edn. CRC Press, 2017.

[41] Yu R, Xue H, Cao Z, *et al*. Effect of oxygen sintering atmosphere on the electrical behavior of CCTO ceramics. *J Eur Ceram Soc* 2012, **32**: 1245–1249.

[42] Lee SY, Kim HE, Yoo SI. Subsolidus phase relationship in the CaO-CuO-TiO_2 ternary system at 950 ℃ in air. *J Am Ceram Soc* 2014, **97**: 2416–2419.

[43] Rahaman MN, Manalert R. Grain boundary mobility of $BaTiO_3$ doped with aliovalent cations. *J Eur Ceram Soc* 1998, **18**: 1063–1071.

[44] Chiang YM, Takagi T. Grain-boundary chemistry of Barium titanate and strontium titanate: I, high-temperature equilibrium space charge. *J Am Ceram Soc* 1990, **73**: 3278–3285.

[45] Li M, Sinclair DC, West AR. Extrinsic origins of the apparent relaxorlike behavior in $CaCu_3Ti_4O_{12}$ ceramics at high temperatures: A cautionary tale. *J Appl Phys* 2011, **109**: 084106.

[46] Nachaithong T, Thongbai P, Maensiri S. Colossal permittivity in $(In_{1/2}Nb_{1/2})_xTi_{1-x}O_2$ ceramics prepared by a glycine nitrate process. *J Eur Ceram Soc* 2017, **37**: 655–660.

[47] Hong SH, Kim DY, Park HM, *et al*. Electric and dielectric properties of Nb-doped $CaCu_3Ti_4O_{12}$ ceramics. *J Am Ceram Soc* 2007, **90**: 2118–2121.

[48] Chung SY, Choi JH, Choi JK. Tunable current-voltage characteristics in polycrystalline calcium copper titanate. *Appl Phys Lett* 2007, **91**: 091912.

[49] Mao P, Wang J, Liu S, *et al*. Improved dielectric and nonlinear properties of $CaCu_3Ti_4O_{12}$ ceramics with Cu-rich phase at grain boundary layers. *Ceram Int* 2019, **45**: 15082–15090.

[50] Cortés JA, Moreno H, Orrego S, *et al*. Dielectric and non-ohmic analysis of Sr^{2+} influences on $CaCu_3Ti_4O_{12}$-based ceramic composites. *Mater Res Bull* 2021, **134**: 111071.

[51] Cotrim G, Cortés JA, Moreno H, *et al*. Tunable capacitor-

varistor response of $CaCu_3Ti_4O_{12}/CaTiO_3$ ceramic composites with SnO_2 addition. *Mater Charact* 2020, **170**: 110699.

[52] Sinclair DC, Adams TB, Morrison FD, *et al*. $CaCu_3Ti_4O_{12}$: One-step internal barrier layer capacitor. *Appl Phys Lett* 2002, **80**: 2153.